DSMC Shock Simulation of Saturn Entry Probe Conditions

Kyle J. Higdon[1]
The University of Texas at Austin, Austin, Texas 78712, USA

Brett A. Cruden[2] and Aaron M. Brandis[3]
AMA, Inc. at NASA Ames, Moffett Field, CA 94035, USA

Derek S. Liechty[4]
NASA Langley Research Center, Hampton, VA 23681, USA

and

David B. Goldstein[5], Philip L. Varghese[6]
The University of Texas at Austin, Austin, Texas 78712, USA

This work describes the direct simulation Monte Carlo (DSMC) investigation of Saturn entry probe scenarios and the influence of non-equilibrium phenomena on Saturn entry conditions. The DSMC simulations coincide with rarefied hypersonic shock tube experiments of a hydrogen-helium mixture performed in the Electric Arc Shock Tube (EAST) at NASA Ames Research Center. The DSMC simulations are post-processed through the NEQAIR line-by-line radiation code to compare directly to the experimental results. Improved collision cross-sections, inelastic collision parameters, and reaction rates are determined for a high temperature DSMC simulation of a 7-species H_2-He mixture and an electronic excitation model is implemented in the DSMC code. Simulation results for 27.8 and 27.4 km/s shock waves are obtained at 0.2 and 0.1 Torr respectively and compared to measured spectra in the VUV, UV, visible, and IR ranges. These results confirm the persistence of non-equilibrium for several centimeters behind the shock and the diffusion of atomic hydrogen upstream of the shock wave. Although the magnitude of the radiance did not match experiments and an ionization inductance period was not observed in the simulations, the discrepancies indicated where improvements are needed in the DSMC and NEQAIR models.

Nomenclature

A, B, C, D	=	parameters in the viscosity integral calculation
a	=	Millikan-White temperature constant
b	=	Millikan-White constant
d_{ref}	=	VHS reference diameter (m)
E_a	=	activation energy (J)
g_j	=	electronic excitation degeneracy at level j
k_b	=	Boltzmann constant ($k_b = 1.3806503\times10^{-23}$ m^2kg/s^2-K)

---

[1] NASA Space Technology Research Fellow, Dept. of Aerospace Engineering and Engineering Mechanics, 1 University Station, C0600, Austin TX, Member AIAA. Contact: khigdon@utexas.edu

[2] Research Scientist, Aerothermodynamics Branch, Associate Fellow AIAA.

[3] Research Scientist, Aerothermodynamics Branch, Senior Member AIAA.

[4] Aerospace Engineer, Aerothermodynamics Branch, Senior Member AIAA.

[5] Professor, Dept. of Aerospace Engineering and Engineering Mechanics, 1 University Station, C0600, Austin TX, Associate Fellow AIAA.

[6] Professor, Dept. of Aerospace Engineering and Engineering Mechanics, 1 University Station, C0600, Austin TX, Associate Fellow AIAA.

K_{eq}	=	reaction rate equilibrium constant
M_{ij}	=	reduced molar weight of a collision pair (g/mol)
n_T	=	number density of the third body partner for a recombination reaction
T_E	=	electron temperature (K)
T_R	=	rotational temperature (K)
T_R^*	=	constant in the Parker rotational collision number equation (K)
T_{ref}	=	reference temperature (K)
T_{Tr}	=	translational temperature (K)
T_V	=	vibrational temperature (K)
Z_R^∞	=	rotational collision number at the high temperature limit
Γ	=	gamma function
$\varepsilon_{el,j}$	=	electronic excitation energy at level j (J)
η	=	temperature exponent in the Arrhenius rate equation
Λ	=	pre-exponential constant in the Arrhenius rate equation (m^3/s)
μ_{ij}	=	viscosity coefficient for a collision pair (kg/m-s)
$\mu_{ij,VHS}$	=	VHS viscosity coefficient for a collision pair (kg/m-s)
σ_R	=	reaction cross-section
σ_T	=	total cross-section
$\sigma_{T,ref}$	=	VHS reference total cross-section (m^2)
$\Omega_{ij}^{(2,2)}$	=	viscosity collision integral for a collision pair (m^2)
ω	=	temperature-viscosity exponent

I. Introduction

RECENT investigations of Saturn entry conditions have been spurred by the high priority listing of Saturn probe missions in the 2013-2022 Decadal Survey for planetary exploration.[1] In prior analysis of the uncertainty present in a CFD simulation of the Saturn entry conditions, it was found that radiative heating may account for up to 20% of peak heating with a large factor of uncertainty.[2] To mitigate this uncertainty, shock tube tests in the Electric Arc Shock Tube (EAST) at NASA Ames Research Center were performed for a range of Saturn entry trajectory conditions.[3] These tests were performed in a hydrogen-helium mixture (89%:11% by volume) for a set of freestream velocities between 25-30 km/s and 0.1-0.5 Torr. The results of these experiments found that quantities in the post-shock region did not reach the expected equilibrium values and that radiative heating may not play a significant role. An induction period occurred in the experiments several centimeters behind the shock where radiance suddenly increased as the electron density increased. In addition, radiance in the vacuum ultra-violet (VUV) range was observed in the pre-shock regions, indicating the diffusion of excited hydrogen upstream of the shock. An attempt was made by Cruden and Bogdanoff to reproduce these observations with existing CFD tools.[2] While successful in generally modeling the electron number density through the shock, the continuum model grossly overpredicts the stagnation line radiance which was attributed to the Boltzmann modeling of excited state populations. Also, the presence of pre-shock radiation and the upstream diffusion of heated gas into the freestream were not captured by the CFD model. A non-continuum method must be applied in order to investigate the mechanisms that result in the pre-shock radiance adequately and to fully characterize the flowfield.

In this work, the direct simulation Monte Carlo (DSMC)[4] technique is utilized to simulate a 1D normal hypersonic shock wave in an 89%:11% H_2-He mixture as measured in the EAST shock tube. This hypersonic shock wave is comparable to the stagnation line quantities experienced during Saturn entry scenarios. To match the DSMC simulations directly to the shock tube experiments, the DSMC results are input to the NEQAIR line-by-line, tangent slab radiation solver in order to calculate radiative quantities.[5] Since radiation is sensitive to the temperature values passed from the DSMC code, the inclusion of an electronic excitation model is necessary. In addition, improved parameters for a 7-species H_2-He mixture (H_2, H, He, H_2^+, H^+, He^+, e^-) are obtained for the various collisional processes modeled in the DSMC simulation. Here, DSMC/NEQAIR simulations of the EAST experiments are performed for two Saturn entry scenarios and radiation spectra are compared to the shock tube results.

II. Approach

A. DSMC Model

The DSMC code used in this work improves on the code base developed by Strand[6] and modified previously by Higdon et al.[7] for the handling of high temperature physics including charged particles. The code is specifically designed to reproduce a 1D unsteady shock wave that develops off of a specular wall. Along with other input parameters, the freestream velocity, number density, and temperature are specified at the outset of the simulation. Once the resultant shock wave has developed and moved far enough away from the wall, a sampling grid that translates with the shock velocity is attached to the shock wave. Macroscopic values such as species number densities, velocities, and temperatures (T_{Tr}, T_R, T_V, T_E) are sampled at various timesteps in order to obtain a quasi-steady representation of the shock wave. Both monatomic and diatomic particles can be handled within the DSMC code, including neutral particles, ions, and electrons. The handling of free electrons is of particular importance because of their relatively small mass compared to the heavy particles. To treat the movement of electrons, Bird's ionization method is employed where quasi-neutrality is assumed such that each electron is constrained to move with a separate ion, but still allowed its own individual energy.[8] When elastic collisions between particles are chosen to occur, the Variable Hard Sphere (VHS) model is utilized to calculate the post-collisional velocities.[9] If a particle is diatomic, an inelastic collision can occur where energy is transferred between the translational, rotational, and vibrational modes through the Larsen-Borgnakke model.[10] For rotational excitation, a continuous distribution represents the internal energy states and Parker's model[11] is used to determine rotational collision number. The simple harmonic oscillator is applied to discretize the vibrational energy distribution and the Millikan and White[12] formula along with Park's[13] high temperature correction is used to calculate the vibrational collision number. In considering chemical reactions, the Total Collision Energy (TCE) model converts Arrhenius reaction rates into reaction cross-sections.[4,9] Since the DSMC code is computationally expensive, it is MPI parallelized to improve efficiency and increase the range of tractable simulation scenarios. Additional details about the DSMC code are available in a recent publication by Higdon et al.[7]

B. Electronic Excitation Model

The modeling of electronic excitation is a crucial step in accurately simulating the ionization process of a high temperature hypersonic shock. Electronic excitation allows particles to climb the electronic energy ladder and obtain enough energy for ionization reactions to occur. In previous studies, several different approaches to handling electronic excitation were proposed. Bird[14], Carlson[15], and Burt[16] all modeled electronic excitation by assuming that each particle contains a distribution of electronic levels based on the equilibrium distribution at the current cell temperature. Ozawa[17] modeled electronic transitions by grouping the electronic levels and treating each excitation as a reaction with a specified reaction rate. In this work, we will follow the electronic excitation model laid out previously by Liechty[18]. Input parameters for the electronic energy and degeneracy of each species' simulated electronic levels are compiled beforehand. From these data, each simulated particle is initialized with a single electronic level sampled from the Boltzmann distribution at the particle's initialization temperature. As particles collide and react, electronic energy transfer is modeled following Larsen-Borgnakke[10] by performing an acceptance-rejection procedure from the equilibrium distribution at the collision energy. The electron temperature (T_E) in the current application of the model is then calculated to be equal to the translational temperature of the free electrons. Note that T_E does not represent the *electronic* temperature, as contributions of the excited states are not taken into account.

C. Radiation Model

The macroscopic quantities output by the DSMC code are useful in order to understand the composition of the flowfield and provide insight into the physics occurring throughout the shock, but radiative spectra are necessary to compare the simulation results to EAST experiments. To calculate the radiative spectra produced by each simulation, the DSMC results are post-processed by passing the species number densities and the translational, rotational, vibrational, and electron temperatures of the bulk fluid to the NEQAIR radiation solver.[5] NEQAIR then calculates the radiance along a line of sight for a uniform slab. The radiative spectra are obtained through a series of line-by-line calculations performed for the participating particle species. Multiple spectral broadening mechanisms are taken into account and spectral and spatial convolutions are included in the final results to mimic the smearing that occurs in experimental measurements. It should be noted that currently, quasi-steady state rates are not yet implemented in the NEQAIR simulations for H atoms. This omission will lead an overestimate of the radiation for non-Boltzmann distributions of the H electronic state populations.

III.   High Temperature H$_2$-He Mixture Parameters

There have been only a few previous DSMC simulations involving H$_2$, H, He, or their ions and, as a result, little time has been spent in providing accurate collision parameters for the models typical to DSMC. The inaccuracies in the few published parameters become even more evident at the high temperatures experienced behind a hypervelocity shock. For this reason, improved DSMC parameters have been tabulated for a 7-species H$_2$-He mixture with a focus on high temperature simulation.

A. VHS Elastic Collisions

For elastic collisions between two particles, previous VHS parameters were published by Bird[4] and Boyd[19]. With the exception of a few of Boyd's parameters, these values for H$_2$ and He are general, collision partner independent fits to low temperature data. In the present work, updated collision integral parameters provided by Palmer, et al.[2] are utilized to obtain high temperature VHS fits. For a collision pair (i, j), the viscosity collision integral, $\Omega_{ij}^{(2,2)}$, is calculated from these parameters (A, B, C, D) in Eq. (1). The viscosity collision integral is then used in Eq. (2) to determine the viscosity coefficient, μ_{ij}, of a neutral collision pair.

$$\Omega_{ij}^{(2,2)} = DT^{A[\ln(T)]^2 + B\ln(T) + C} \tag{1}$$

$$\mu_{ij} = 2.6693 \times 10^{-6} \frac{\pi\sqrt{M_{ij}T}}{\Omega_{ij}^{(2,2)}} \tag{2}$$

Species specific VHS parameters for $\sigma_{T,ref}$ and ω were obtained for neutral-neutral and charge-neutral collisions by least squares curve fitting $\log(\mu_{ij})$ to the log of the VHS viscosity coefficient, $\mu_{ij,VHS}$, shown in Eq. (3). This equation takes the form of the first approximation of the Chapman-Enskog viscosity coefficient for a VHS gas and is described by Bird.[20]

$$\mu_{ij,VHS} = \frac{\frac{15}{2}\sqrt{\pi m k_b}T^\omega}{(5 - 2\omega)(7 - 2\omega)\sigma_{T,ref}T_{ref}^{(\omega - \frac{1}{2})}} \tag{3}$$

To perform the curve fit, a reference temperature of 1000 K was chosen and discrete points were taken from Eq. (2) ranging from 100 to 10,000 K.

Since the scope of the VHS model is limited to two parameters, the model cannot capture the Coulombic forces present in charge-charge interactions. In these cases, charge-charge collision parameters are assumed to be identical to the charge-neutral parameters. This introduces some error, but this is considered to be acceptable because charge-charge collisions are relatively rare in the current simulations. Table 1 compiles the fitted high temperature parameters for the H$_2$-He mixture where the VHS reference diameter, d_{ref}, is calculated from the reference cross-section. An example of one of the curve fits is shown in Figs. 1 and 2 for a H$_2$-H$_2$ elastic collision. Figure 1 compares the calculation of the viscosity coefficient with the current VHS fit to previous VHS parameters determined by Bird[4] and Boyd[19]. In addition, it shows the viscosity calculated from Eqs. (1) and (2) using parameters from Palmer's review of the viscosity coefficient.[2] Discrete points were selected from this line to determine the current fit shown in Fig. 1. At very high temperatures, the current fit starts to diverge from Palmer's viscosity and the discrepancy between the fit and the calculated viscosity grows as even higher temperatures are reached. This error at very high temperatures is acceptable as evidenced in Fig. 2. The variance in the collision cross-section is small at high temperatures so that the effect on simulations in this temperature range will be minimal.
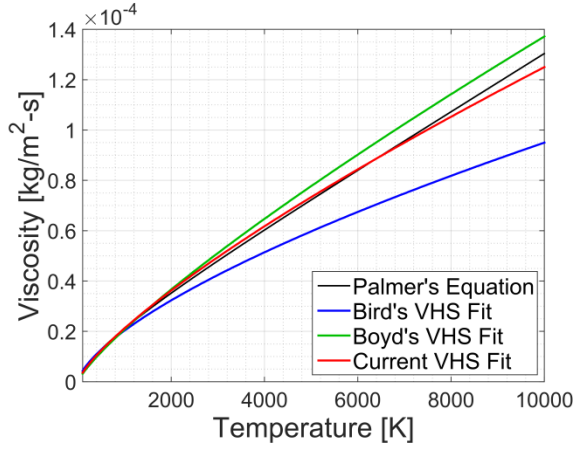
Figure 1. H₂-H₂ viscosity coefficient curve fit of VHS parameters to Palmer's empirical data and comparisons with other published VHS parameters.
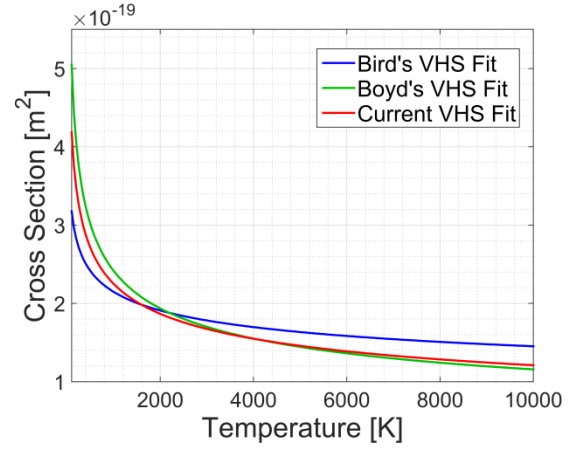

Figure 2. H₂-H₂ VHS cross-section for the current curve fit compared with other published VHS parameters.

Table 1. 7-species H₂-He VHS cross-section parameters at T_{ref} = 1000.

	H₂	H	He	H₂⁺	H⁺	He⁺	e⁻
	ω, d_{ref} [10^{-10} m]						
H₂	0.770, 2.678	0.927, 2.581	0.775, 2.462	0.907, 3.883	0.880, 3.912	0.982, 3.874	0.400, 1.695
H	-	0.825, 2.913	0.859, 2.396	0.905, 3.639	1.006, 5.642	0.912, 2.865	0.831, 3.689
He	-	-	0.759, 2.137	0.761, 2.657	0.974, 3.029	0.855, 3.535	0.510, 1.380
H₂⁺	-	-	-	0.907, 3.883	0.880, 3.912	0.982, 3.874	0.400, 1.695
H⁺	-	-	-	-	1.006, 5.642	0.912, 2.865	0.831, 3.689
He⁺	-	-	-	-	-	0.855, 3.535	0.510, 1.380
e⁻	-	-	-	-	-	-	-

B. Inelastic Collisions

When inelastic collisions involving H₂ occur, collision numbers for rotational and vibrational relaxation are calculated to determine the probability of a relaxation event. A review of vibrational collision number correlations is presented by Palmer[2], and a refit for the Millikan-White formula[12] was provided. These refit parameters will be used in the following simulations (Table 2). The applicability of rotational collision number values is not as straight-forward. The modeling of rotational energy exchange is well developed in DSMC. Unfortunately, diatomic hydrogen is unlike any of the various molecular species typically modeled by DSMC. Usually, the probability of rotational exchange decreases with increasing temperature and simulation of this trend is often handled with Parker's model[11] for calculating the rotational collision number, Z_R^{∞}. Experiments at low temperatures for diatomic hydrogen have shown that the reverse trend is actually true. It has been shown in a previous study by Boyd (1994) that the rotational collision number actually decreases with increasing temperature in the low temperature regime.[21] Boyd proposed a relationship between the rotational collision number and the temperature, but this model is only valid for low temperatures. Figure 3 presents a large set of collision numbers compiled from various sources for a moderate temperature range between 200 and 1500 K.[22] The data in this region are inconsistent and do not follow any identifiable trends so it is unclear whether this lack of consistency continues into high temperatures. For this reason, a constant collision number, Z_R^{∞}=174, is "fit" to the existing data. Even, though this may be a poor representation of the rotational collision number, diatomic hydrogen dissociates relatively quickly in high temperature flows so accurate modeling of rotational relaxation may not be particularly important. As with elastic collisions, the equivalent vibrational and rotational parameters are utilized for the diatomic ions.
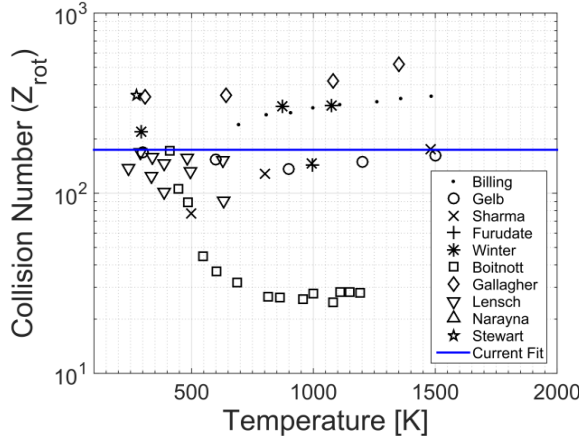
Figure 3. Rotational collision number curve fit to compiled experimental and empirical data.

Table 2. Diatomic species rotational and vibrational parameters.

Species	Z_R^∞	T_R^* [K]
H_2	174	0.0

Collision Pair	a	b
H_2-H_2	65.110	0.006821
H_2-H	9.673	0.07250
H_2-He	69.971	0.004682

C. Arrhenius Reaction Rates

Forward reaction cross-sections for the H_2-He mixture are calculated in the TCE model through Arrhenius reaction rates tabulated by Leibowitz.[23] Most CFD simulations calculate reverse reaction rates directly from the equilibrium constant, K_{eq}, but applying a reverse reaction rate in DSMC is not as simple. Since the TCE model requires an Arrhenius form to calculate reaction cross-sections, the reverse Arrhenius reaction rates must be fit to the ratio of the forward rate to the equilibrium constant and then curve fitted to Arrhenius form. In addition to restrictions imposed by the Arrhenius form, the TCE model also imposes limits to the Arrhenius parameters. All of the reverse reaction rates that are required for this set are termolecular reactions where the reaction probability from the TCE model is calculated as

$$\left(\frac{\sigma_R}{\sigma_T}\right)_k = \frac{\sqrt{\pi} n_T \varepsilon \Lambda T_{ref}^\eta}{2\sigma_{ref}} \frac{\Gamma(\frac{5}{2} - \omega)}{\Gamma(\eta + \frac{3}{2})} \sqrt{\frac{m_r}{2k_b T_{ref}}} \left(\frac{E_c}{k_b T_{ref}}\right)^{\eta - 1 + \omega} \tag{4}$$

where $\varepsilon = 1$ if $i \neq j$ or $\varepsilon = 2$ if $i = j$, m_r is the reduced mass of i and j, E_c is the total collision energy, n_T is the number density of the third body, σ_{ref}, T_{ref}, and ω are the VHS parameters for species i and j, and Λ, η, E_a are from the Arrhenius reaction rate equation. In Eq. (4), the activation energy, E_a, in the Arrhenius equation is assumed to be zero which reduces the number of available curve fit parameters to two.

Using the remaining Arrhenius equation parameters and equilibrium constants taken from Lewis[24], a least-squares fit was performed on the log of the reverse reaction rates. The complete set of forward and reverse Arrhenius reaction rates is shown in Table 3. In order to obtain the most accurate reverse Arrhenius rates, the recombination reactions were fit to a temperature range between 5,000 to 20,000 K unless otherwise noted. Figures 4 and 5 show K_{eq} and the reverse reaction rate for the $H + H + H_2 \rightarrow H_2 + H_2$ reaction. Relatively good agreement is obtained for both the Lewis[24] and Park[25] equilibrium constants in the region of interest, but at high temperatures the rate is severely over-predicted. The curve fits for the reverse two-step ionization (electron capture) reactions suffer even more from the limitations of the TCE model. Consider the reverse reaction, $H^+ + e^- + H \rightarrow H + H$, which was also fit between 5,000 to 20,000 K (Figs. 6 and 7). In this region, the reaction rate calculated from the equilibrium constant decreases rapidly as the temperature increases. Since the reaction probability must then decrease with increasing temperature, Eq. (4) requires that the Arrhenius temperature exponent must satisfy $\eta < 1 - \omega$ leading to the limitation that $\eta < 0.175$ for the two-step electron capture reaction. In addition to this limit, the Arrhenius temperature exponent must be large enough that the gamma function input in the denominator of Eq. (4) is greater than zero which requires that > -1.5 . This lower limit causes problems for fitting this two-step electron capture reaction because the "ideal" Arrhenius temperature exponent curve fit value is approximately –5.0. To address this issue, a value for η is specified for the reaction rates that do not satisfy the constraints of the TCE model. Although an Arrhenius temperature exponent of –1.5 would provide the best fit to the equilibrium constant, the reaction probability calculated from Eq. (4) would be zero at all temperatures. Instead, a minimum value was specified at

$\eta = -1.0$ for all of the two-step electron capture reactions. This leaves just one parameter from Eq. (4), the Arrhenius pre-exponential constant (Λ), to fit to the reverse reaction rate and leads to the gross errors demonstrated in Figs. 6 and 7. Although recombination reactions are relatively rare and should not have a significant effect on the overall results, the poor reaction rate fitting may lead to discrepancies in the equilibrium concentration and could affect the production rate in non-equilibrium regions. Note that there are currently no reaction rates involving creation of H_2^+ meaning that this species will not be produced unless a simulation is initialized with H_2^+. The ionization energy of H_2 is 15.42 eV which is not much higher than the 13.6 eV for H, but H_2^+ should only play a minor role as diatomic hydrogen is dissociated rapidly at the high temperatures simulated in this study. In the future, reaction rates for H_2^+ will be investigated.
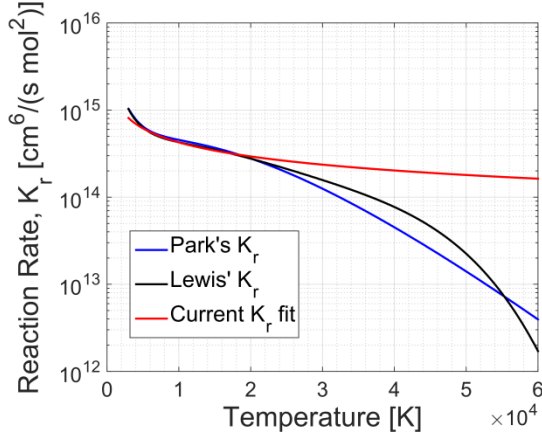

Figure 4. Reverse reaction rate curve fit to Lewis' rate and comparisons to reverse reaction rates calculated from the Park and Lewis equilibrium constants for $H + H + H_2 \rightarrow H_2 + H_2$.
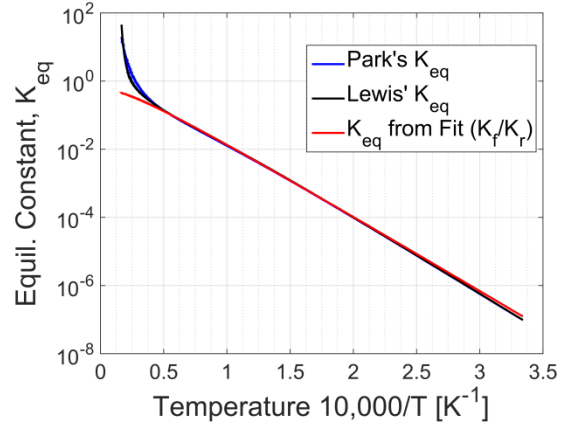

Figure 5. K_{eq} calculated from the curve fit compared with Lewis' and Park's K_{eq} expression for $H + H + H_2 \rightarrow H_2 + H_2$.
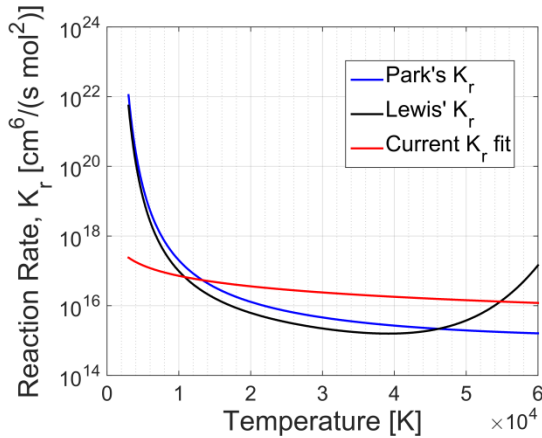

Figure 6. Reverse reaction rate curve fit to Lewis' rate and comparisons to reverse reaction rates calculated from the Park and Lewis equilibrium constants for $H^+ + e^- + H \rightarrow H + H$.

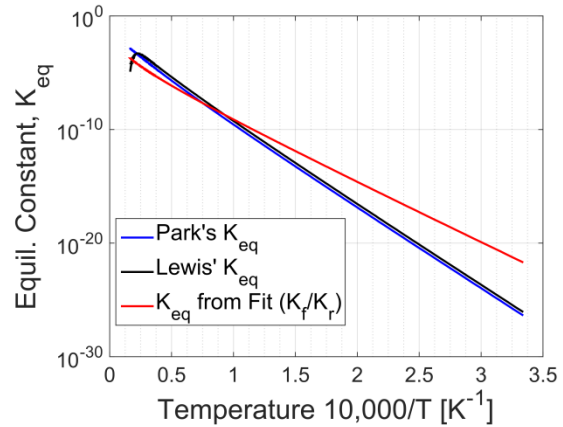**Figure 7. K_{eq} calculated from the curve fit compared with Lewis' and Park's K_{eq} expression for $H^+ + e^- + H \rightarrow H + H$.**

American Institute of Aeronautics and Astronautics

Table 3. H$_2$-He mixture reaction rates.

#	Reaction	Forward Rate Coefficients			Backward Rate Coefficients		
		Λ [m^3/s]	η	E_a [10^{-19} J]	Λ [m^3/s]	η	E_a [10^{-19} J]
1	H$_2$ + H$_2$ $\rightleftharpoons$ H + H + H$_2$	1.727×10^{-11}	-1.0	7.17358	1.6248×10^{-43}	-0.535	0.0
2	H$_2$ + H $\rightleftharpoons$ H + H + H	1.386×10^{-10}	-1.0	7.17358	1.3040×10^{-42}	-0.535	0.0
3	H$_2$ + He $\rightleftharpoons$ H + H + He	6.924×10^{-12}	-1.0	7.17358	6.5143×10^{-44}	-0.535	0.0
4	H$_2$ + H$_2^+$ $\rightleftharpoons$ H + H + H$_2^+$	1.727×10^{-11}	-1.0	7.17358	1.6248×10^{-43}	-0.535	0.0
5	H$_2$ + H$^+$ $\rightleftharpoons$ H + H + H$^+$	1.386×10^{-10}	-1.0	7.17358	1.3040×10^{-42}	-0.535	0.0
6	H$_2$ + He$^+$ $\rightleftharpoons$ H + H + He$^+$	6.924×10^{-12}	-1.0	7.17358	6.5143×10^{-44}	-0.535	0.0
7	H$_2$ + e$^-$ $\rightleftharpoons$ H + H + e$^-$	1.386×10^{-10}	-1.0	7.17358	1.3040×10^{-42}	-0.535	0.0
8[*]	H + H $\rightleftharpoons$ H$^+$ + e$^-$ + H	1.024×10^{-19}	0.5	16.0293	1.9848×10^{-39}	-1.0	0.0
9[*]	H + He $\rightleftharpoons$ H$^+$ + e$^-$ + He	8.103×10^{-20}	0.5	16.0293	1.5706×10^{-39}	-1.0	0.0
10[†]	H + e$^-$ $\rightleftharpoons$ H$^+$ + e$^-$ + e$^-$	3.790×10^{-17}	0.5	21.7866	1.2614×10^{-38}	-0.978	0.0
11[*]	H + e$^-$ $\rightleftharpoons$ H$^+$ + e$^-$ + e$^-$	6.830×10^{-17}	0.5	16.0293	1.3228×10^{-36}	-1.0	0.0
12[‡]	He + e$^-$ $\rightleftharpoons$ He$^+$ + e$^-$ + e$^-$	2.210×10^{-17}	0.5	39.3899	2.0319×10^{-39}	-0.989	0.0
13[*]	He + e$^-$ $\rightleftharpoons$ He$^+$ + e$^-$ + e$^-$	3.720×10^{-17}	0.5	32.0449	5.2089×10^{-37}	-1.0	0.0

*Two-step process where particle is excited to first state and then immediately ionized by a second collision.

† Reverse reaction curve fit between 5,000-25,000 K.

‡Reverse reaction curve fit between 5,000-40,000 K.

D. Electronic Excitation Levels

The calculation of electronic excitation is relatively straightforward for the model used in our DSMC simulation. Appendix A contains a set of tabulated electronic level degeneracies and energy values compiled from the NIST database[26]. Currently, this set is as complete as possible with the available information from NIST. Electronic excitation values for H$_2^+$ are not available as the excited electronic states are predissociated and H$^+$ does not contain an electron to excite. The omission of H$_2^+$ excitation should have a negligible effect on the results of any high temperature simulation since diatomic hydrogen is expected to dissociate immediately once excited.

IV. Results

In this section, we apply the new models and input parameters from Sections II and III to the DSMC simulations. First, we compute a 0-dimensional relaxation to validate that the physics simulated in our DSMC model reproduces equilibrium. Next, we compare the results of our DSMC simulations of a 1-dimensional hypersonic shock tube to two experiments performed in EAST. Due to the experimental setup constraints, high speeds, and high temperatures observed, data collected from this work focused on spectral analysis of the flow. Since our DSMC code does not explicitly calculate radiation, the NEQAIR line-by-line radiation code[5] is utilized to post-process the DSMC results and obtain a representation of the emission spectrum which is directly compared to the experimental results.

A. 0-Dimensional Relaxation

Before a full simulation of a hypersonic shock wave in a H$_2$-He mixture is performed, it is worthwhile to assess the addition of the new models and parameters to our DSMC code. To simply demonstrate various models, a 0-dimensional simulation was completed for the relaxation of a Saturn atmospheric mixture of 89%:11% H$_2$-He at 0.2 Torr towards an equilibrium temperature. Instead of initializing all the temperatures with a single value, the translational temperature was initialized at 20,000 K and the rotational, vibrational, and electronic temperatures were initialized at 300 K. In this simulation, all of the particle models, including chemical reactions, were enabled and the temperatures were allowed to relax until equilibrium was reached (Fig. 8). The diatomic hydrogen begins to dissociate rapidly and the temperatures equilibrate quickly with each other as seen by the inset box in Fig. 8. Because the rotational collision number is independent of temperature, it is initially relaxes slower than the vibrational temperature and as the temperatures approach equilibrium with each other, rotational relaxation overtakes vibrational relaxation. Even though the temperatures equilibrate with each other relatively quickly, the relaxation process occurs over a much longer timescale due to the persistence of slow hydrogen-helium chemistry. The expected equilibrium temperature was calculated from the Chemical Equilibrium with Applications code[27] and
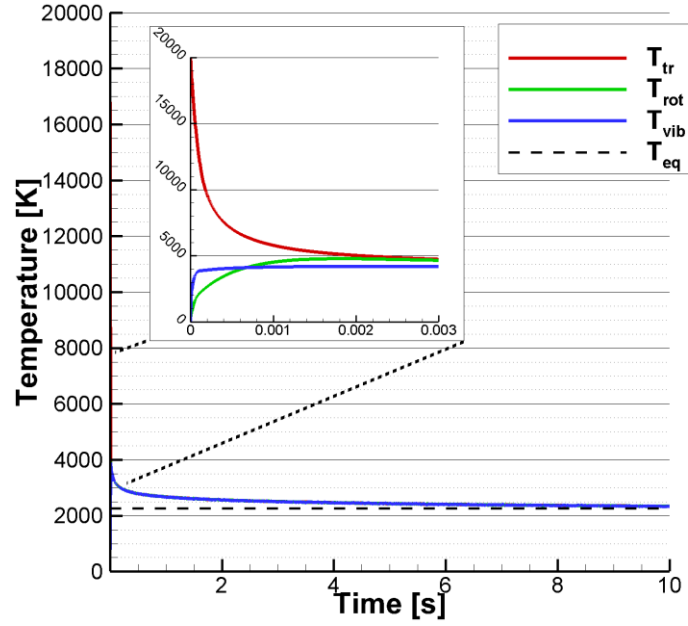
Figure 8. 0-D relaxation of a gas initialized at $T_{tr}=20,000$.

Table 4. Inflow conditions for the scenarios considered here.

Case	EAST Shot 25	EAST Shot 17
Shock velocity (km/s)	27.8	27.4
Number density (#/m^3)	6.4377×10^{21}	3.2189×10^{21}
Temperature (K)	300	300
H$_2$ mole fraction (%)	89	89
He mole fraction (%)	11	11

is represented by the dashed line in Fig. 8. By approximately 10 seconds, the simulated temperature and mole factions (not shown here) have obtained the expected equilibrium values.

B. EAST Shot 25 Simulation

Having tested the DSMC code on a 0-dimensional relaxation, it was next applied to simulate Shot 25 from a recent campaign in the EAST for Saturn entry conditions.[3] The inflow conditions simulated in this scenario are listed in Table 4 and DSMC shock results are shown in Figs. 9-10 for EAST Shot 25 which had an initial pressure of 0.2 Torr and reached a shock velocity of 27.8 km/s. The output quantities are ensemble averaged as the DSMC sampling domain moves with the shock and the shock location is defined as $X = 0$. The solid lines in Fig. 9 show the variation of particle number densities with respect to distance from the shock wave and the solid lines in Fig. 10 plot the total translational, rotational, vibrational, and electron temperatures through the shock wave. Diatomic hydrogen becomes scarce behind the shock due to high temperature dissociation and by approximately 1.5 cm, H$_2$ has completely dissociated. Neither He$^+$ nor H$_2^+$ are produced in this scenario, but the number density of the atomic hydrogen ions and electrons increases rapidly behind the shock and is on the order of the helium number density downstream as the flow approaches equilibrium. The electron and atomic hydrogen ion number densities are identical in this simulation so the black and magenta lines overlay each other in Fig. 9. Charged species make up less than 10% of the total number of particles, but modeling this ionization is important for the calculations of radiation and comparisons to experimental measurements. Since there is only a small degree of ionization, the assumption of charge neutrality is acceptable which validates our selection of Bird's[8] electron movement model.

In Ref. 3, Cruden estimated the electron number density from Stark analysis and found the number density to be approximately 1.0×10^{21} m^{-3} at 1.4 cm behind the shock. This number density value is determined from a low

resolution Balmer-γ line measurement with a large uncertainty. Cruden found that at about 3 cm, the electron number density is increasing, but does not quite reach the equilibrium value of roughly 4.2×10^{21} m^{-3} by 5 cm. In Fig. 9, the electron number density is seen to be slightly greater than the Ref. 3 value at 1.4 cm and increasing rapidly. By 5 cm, the electron number density in Fig. 9 is already larger than the expected equilibrium value and Fig. 10 proves that equilibrium has not yet been reached at this point. The temperatures equilibrate to each other behind the shock, but the ionization process is still occurring and the system has not yet reached full equilibrium by 5 cm behind the shock. The poor electron number density comparison and overshoot of equilibrium can most likely be attributed to errors in the curve fitted reverse reaction rates, particularly the electron capture rates, and the misrepresentation of the corresponding equilibrium constant.

In addition to comparisons with analyses of the experimental results, the DSMC simulation of Shot 25 can be directly equated to the experimental data by processing the output through NEQAIR to obtain emission spectra. Figs. 11-14 compare the experimental results to the convolved output from the radiation solver in the VUV, ultra-violet (UV), visible, and near-infrared (IR) spectral ranges. All four ranges detect emission due to various transitions from excited atomic hydrogen states along with Lyman band emission from molecular hydrogen in VUV. The simulated molecular and Lyman-α emission in the VUV range (Fig. 11) occurs post-shock where we expected to see pre-shock emission from heated H. The Lyman-α emission occurs from electronically excited H transitioning from the n=2 orbital to the n=1 orbital. Slight diffusion of atomic H is seen upstream of the shock in Fig. 9. Although not definitive, this generally agrees with the observations of Lyman-α radiation in the pre-shock region which Cruden[3] concluded was due to atomic hydrogen diffusing upstream of the shock. In Ref. 3, it was determined that optically thick radiation would be seen for atomic hydrogen number densities as low as 1.0×10^{18} m^{-3}. The DSMC simulation predicts H number densities this large as far as 1.2 cm upstream of the shock suggesting again that this upstream H could be emitting if it is hot enough.

It is apparent in Figs. 11-14 that the simulated results currently over-predict the radiance throughout most of the measured region. In addition, the delayed radiative transition (or induction time) experienced in the EAST experiments is not observed in the simulation. Figure 14 shows drastic difference between the experimental and calculated emission from the near-IR Paschen lines and there seems to be little agreement between the two results. On the other hand, the simulated radiance in Figs. 12 and 13 seem to reproduce the correct magnitude and shape, but the simulated radiance occurs several centimeters before the experiment's radiance. Regardless, it is encouraging that the radiance measurements are of the correct shape and rough order of magnitude compared to the experimental data for these two ranges. The current discrepancies may be due to several factors including the omission of ambipolar diffusion, the use of Boltzmann distributed electronic state populations for H atoms in NEQAIR, inaccurate high temperature data for the H$_2$-He mixture, or misrepresentation of the electronic temperature input into NEQAIR. The use of an incorrect electronic temperature input to NEQAIR is the most likely culprit in missing the upstream Lyman-α emission. As stated earlier, the simulated electronic temperature is determined from the kinetic energy of the electrons such that the *electronic* temperature and *electron* temperature are assumed equal. Since electrons are not present upstream of the shock, the electronic temperature in this region is undefined. This representation of the electronic temperature does not take into account the fact that excited hydrogen has diffused upstream of the shock. With the implementation of a temperature model that combines both the kinetic electron energy and the excited states of the particles, NEQAIR should predict Lyman-α emission in this upstream region.

In order to demonstrate the importance of including electronic excitation in the DSMC model for high temperature flows, Figs. 9-14 compare simulations with and without the electronic excitation model. The most drastic improvement is seen in Fig. 9 where the number density of the charged species has increased by nearly two orders of magnitude. In turn, this has an effect on the radiation produced by the NEQAIR code. In addition, the translational and electron temperatures continue decreasing post-shock, presumably because the chemical reactions and electronic energy distributions approach equilibrium. When comparing the effects on the radiance of including electronic excitation in the DSMC code (Figs. 11-14), the improvement in the magnitude and shape of the downstream region of the emission calculation is encouraging.
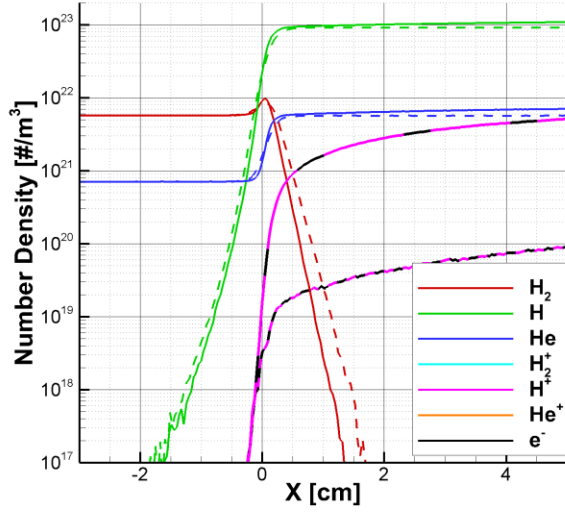
Figure 9. Simulated particle number densities including electronic excitation (solid) and without electronic excitation (dashed) relative to the shock location for EAST Shot 25.
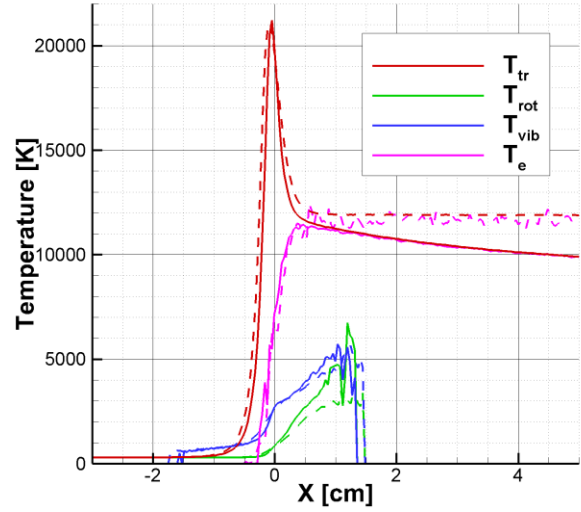

Figure 10. Simulated bulk temperatures including electronic excitation (solid) and without electronic excitation (dashed) relative to the shock location for EAST Shot 25.
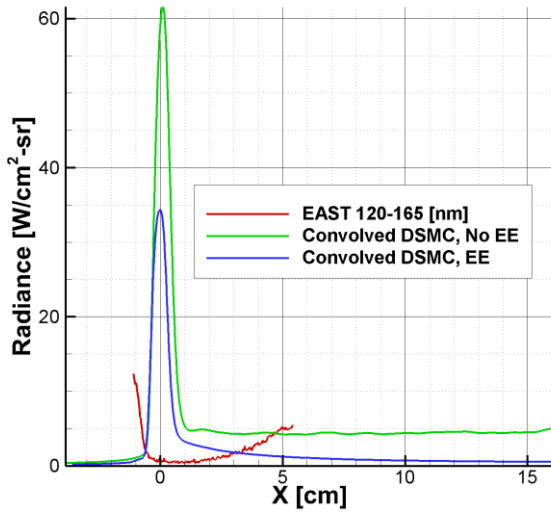

Figure 11. Simulated radiance with and without electronic excitation in the VUV range relative to the experimental data for EAST Shot 25.
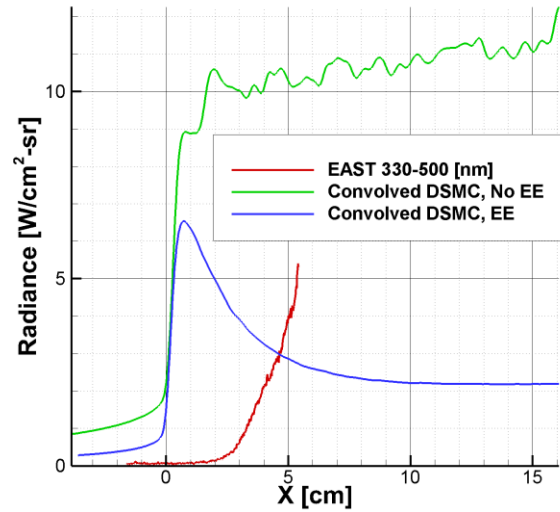

Figure 12. Simulated radiance with and without electronic excitation in the UV range relative to the experimental data for EAST Shot 25.
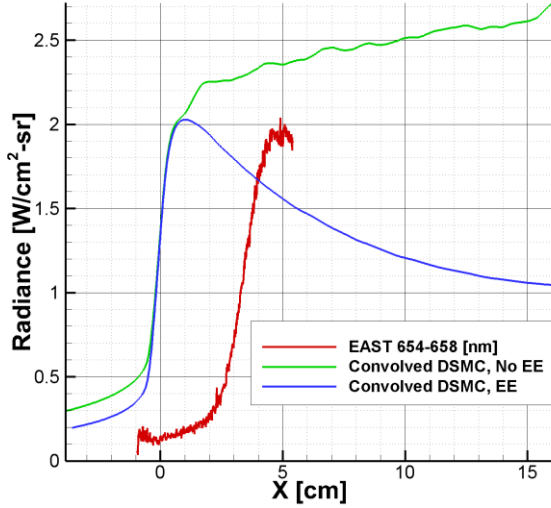
Figure 13. Simulated radiance with and without electronic excitation in the visible range relative to the experimental data for EAST Shot 25.
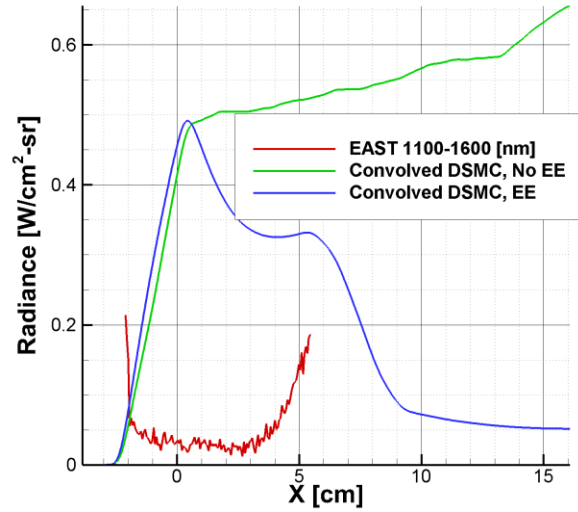

Figure 14. Simulated radiance with and without electronic excitation in the near-IR range relative to the experimental data for EAST Shot 25.

C. EAST Shot 17 Simulation

To compare our results to a lower density experiment, we used the DSMC model to simulate Shot 17 from the same experimental campaign in the EAST shock tube. Figures 15 and 16 show the simulated number densities and temperatures as a function of the spatial location relative to the shock for a velocity of 27.4 km/s and initial gas pressure of 0.1 Torr. The length until complete dissociation of H_2 is nearly three times larger than for Shot 25 and no ions besides H^+ are present downstream. In this shot, α line measurements were used by Cruden[3] to calculate a constant electron density of approximately 5.0×10^{20} m^{-3} throughout the post-shock region, though the actual values may have been lower due to resolution limitations. In Ref. 3, the equilibrium electron number density was determined to be 2.0×10^{21} m^{-3}. The electron number density in Fig. 15 is fairly consistent with the measured experimental number density, but demonstrates a gradually increasing trend. This trend continues downstream and appears to be approaching the equilibrium number density value. Investigation further downstream showed that the electron number density surpasses the equilibrium value and this is again attributed to the incorrect reverse reaction rates. As was seen in Shot 25, atomic hydrogen diffuses upstream of the shock, but in this case the diffusion distance is much longer. To support our previous claim that this hydrogen is hot and the cause of the Lyman-α band emission seen in the simulations, the translational temperature of H is plotted in Fig. 16. The pre-shock temperature of atomic hydrogen is between 20,000-25,000 K and is hot enough to electronically excite the hydrogen, indicating again that an improved representation of the electronic temperature should produce more accurate results in modeling the Lyman-α radiance.

After post-processing the DSMC results with NEQAIR and convolving the radiance with the instrument line functions, simulated emission profiles for the VUV, UV, and visible wavelengths were produced (Figs. 17-19). As in Shot 25, the magnitude of the radiance does not agree with the experimentally measured values. In the VUV range (Fig. 17), the width of the spike is comparable to the measured radiance although this peak again occurs at the shock front instead of in the pre-shock region. The onset of modeled radiance in the UV range seems to follow the same trend as the experimental data, but we again see a shift in where emission begins. Similarities between the simulation and experiment are more difficult to determine in the visible range, but the radiance increases at the shock front for both sets.
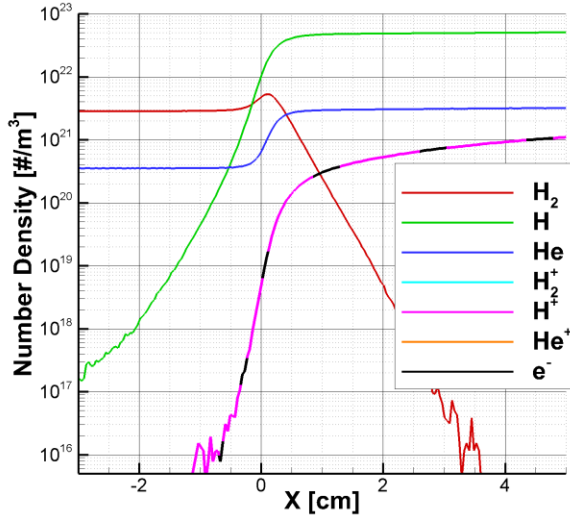
Figure 15. Particle number densities relative to the shock location for EAST Shot 17.
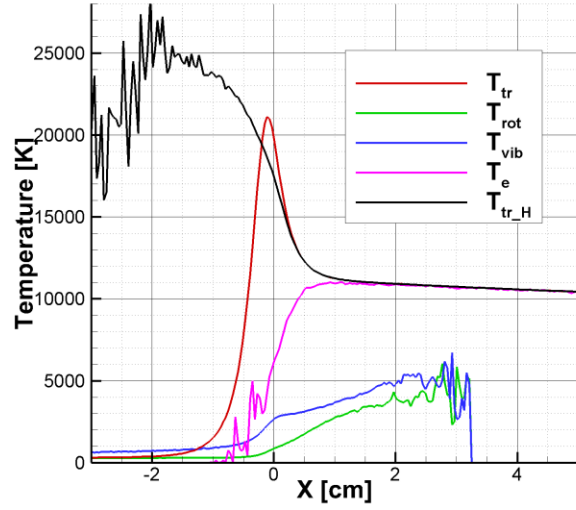

Figure 16. Bulk temperatures relative to the shock location for EAST Shot 17.
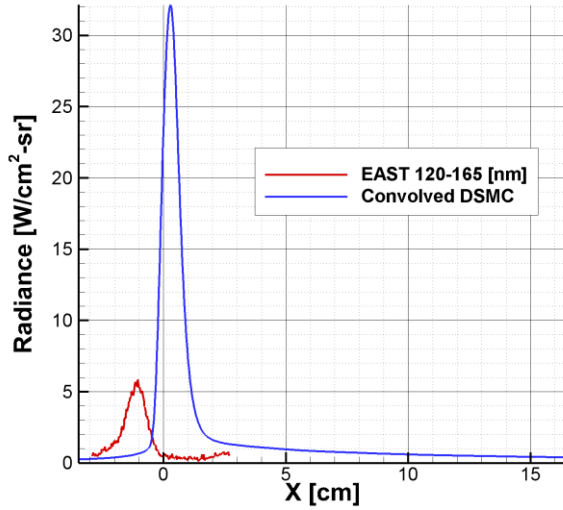

Figure 17. Radiance in the VUV range relative to the shock location for EAST Shot 17.
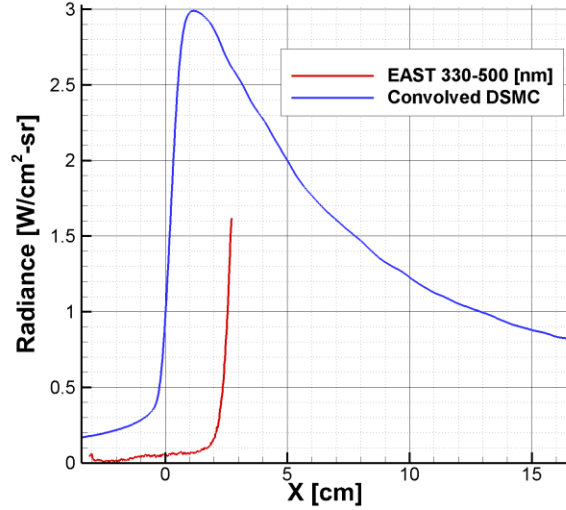

Figure 18. Radiance in the UV range relative to the shock location for EAST Shot 17.
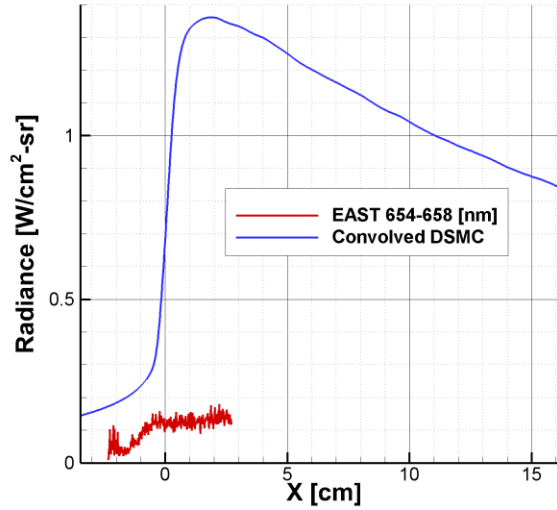
Figure 19. Radiance in the visible range relative to the shock location for EAST Shot 17.

V. Conclusions

This work represents a first attempt at reproducing hypersonic shock tube experiments for a H_2-He mixture with DSMC. Before simulations could be performed, the implementation of Liechty's electronic excitation model[18] was completed and input parameters for the VHS, Larsen-Borgnakke, Arrhenius, and electronic excitation models were fitted or compiled. Care was taken to fit model parameters to high temperature data where possible in order to improve the accuracy of the physics in the high temperature scenarios of interest. Large discrepancies in the two-step electron capture reaction rate were found to be necessary for application in the current TCE model. Demonstration of expected equilibrium using these new parameters was tested by reproducing equilibrium after a 0-dimensional relaxation. In a 1-dimensional shock wave study, the inclusion of an electronic excitation model was shown to have drastic effects on the charged particle number densities and post-shock temperature. In turn, this improved the comparison of the DSMC results to the experimental data.

Two EAST hypersonic shock tube experiments for Saturn entry were simulated with our DSMC code. To compare the simulations directly to the experimental measurements of the emission radiance, the DSMC results were post-processed through the NEQAIR line-by-line radiation code. When comparing to the experiments, we found that the simulated radiance typically had a much greater magnitude, but that the profiles were sometimes qualitatively similar to the experimental results. The DSMC simulation was consistent with the experimental observations in that equilibrium was not obtained by the end of the sampling region. In the experiments, an inductance time was observed before the onset of radiation. There was no indication that this inductance time was present in the DSMC simulations. This discrepancy was again seen when comparing the number density of electrons through the shock to the experiments and is possibly due to the post processing of the DSMC code with a Boltzmann radiation model and/or incorrect reverse reaction rates. The relative magnitudes of the electron number density were similar, but the trends did not match between simulation and experiment. We were able to confirm the experimental observation that atomic hydrogen diffuses upstream of the shock, although we did not see emission of the Lyman-α band in the upstream region. This could be explained by our representation of the electronic temperature as purely the translational temperature of the free electrons, but needs to be investigated further. Since free electrons are not present upstream, the electronic temperature is undefined and NEQAIR could not yield spectra. In analyzing the translational temperature of the atomic hydrogen upstream of the shock, it is obvious that these high temperature particles should be emitting in this region. Overall, this work was able to answer some key questions about the physics observed in the EAST experiments and we were able to identify areas where advancements in simulating physics should improve comparisons with the measured data. Deficiencies identified in these Saturn entry simulations could guide model selection for other simulations such as Earth entry. For example, the H_2-He mixture could be studied to determine the importance of ambipolar diffusion in calculating shock radiation and its structure.

In the future, several improvements and analyses of the simulations can be implemented. A new representation of the electronic temperature will be executed which includes both the electron temperature and the energy in the electronically excited levels. Since the presence of electrons is critical to the production of spectra in the NEQAIR

14

American Institute of Aeronautics and Astronautics

code, modeling ambipolar diffusion may have an effect on the results. Ambipolar diffusion would cause the electrons and ions to diffuse further upstream which could potentially allow the emission from the hot atomic hydrogen upstream to be seen. On the other hand, it would lead to earlier ionization, making the distance between the simulated ionization location and the experimental inductance even greater. The correct ionization rate and charged particle number density could be obtained with a more sophisticated model for calculating reaction probabilities. In addition, an improved temperature dependent model for rotational relaxation of H_2 should be developed for high temperatures although it may not have significant effects in this simulation. The inclusion of quasi-steady state rates for H in NEQAIR could also reduce the difference in radiative magnitude by more accurately representing the non-equilibrium present. Once the most critical improvements have been completed, a global sensitivity analysis can be performed for the improved H_2-He parameters used in the DSMC simulation. A previous sensitivity analysis was performed for an 11-species air case[7] so the resources to complete this task are readily available. The sensitivity analysis would be performed encompassing a number of DSMC parameters such as the Arrhenius reaction rates, VHS cross-sections, and simulation parameters. We can then quantify the sensitivity of each of the parameters and rank them in order of importance to some quantity of interest. This will be a significant step for identifying the most important input parameters in the system and for future research where we can select the highest ranked parameters and calibrate them to the EAST data with a Markov Chain Monte Carlo method.

Acknowledgments

References

[1]National Research Council, *Vision and Voyages for Planetary Science in the Decade 2013-2022*, National Academies Press, 2012.

[2]Palmer, G., Prabhu, D., and Cruden, B. A., "Aeroheating Uncertainties in Uranus and Saturn Entries by the Monte Carlo Method," *Journal of Spacecraft and Rockets*, Vol. 51, No. 3, 2014, pp. 801-814.

[3]Cruden, B. A., and Bogdanoff, D. W., "Shock Radiation Tests for Saturn and Uranus Entry Probes," *45th AIAA Thermophysics Conference*, AIAA Paper No. 2015-2965, Dallas, TX, 2015.

[4]Bird, G. A., *Molecular Gas Dynamics and the Direct Simulation of Gas Flows*, Clarendon Press, Oxford, 1994.

[5]Cruden, B. A., and Brandis, A. M., "Updates to the NEQAIR Radiation Solver," *Radiation in High Temperature Gases*, St. Andrews, UK, 2014.

[6]Strand, J.S., "Statistical Methods for the Analysis of DSMC Simulations of Hypersonic Shocks," Ph.D. Dissertation, Dept. of Aerospace Engineering, The University of Texas at Austin, Austin, TX, 2012.

[7]Higdon, K. J., Goldstein, D. B., and Varghese, P. L., "Sensitivity Analysis of DSMC Parameters for Ionizing Hypersonic Flows," *45th AIAA Thermophysics Conference*, AIAA Paper No. 2015-3371, Dallas, TX, 2015.

[8]Bird, G. A., "Direct Simulation of Typical AOTV Entry Flows," *AIAA and ASME Fourth Joint Thermophysics and Heat Transfer Conference*, AIAA Paper No. 86-1310, Boston, MA, 1986.

[9]Bird, G. A., "Monte Carlo Simulation in an Engineering Context," in *Rarefied Gas Dynamics*, edited by S. S. Fisher, AIAA, New York, Part 1, 1981, pp. 239-255.

[10]Borgnakke, C. and Larsen, P. S., "Statistical Collision Model for Monte Carlo Simulation of Polyatomic Gas Mixture," *Journal of Computational Physics*, Vol. 18, Issue 4, 1975, pp. 402-420.

[11]Parker, J. G., "Rotational and Vibrational Relaxation in Diatomic Gases," *Physics of Fluids*, Vol. 2, No. 4, 1959, pp. 449-462.

[12]Millikan, R. C., and White, D. R., "Systematics of Vibrational Relaxation," *Journal of Chemical Physics*, Vol. 39, 1963.

[13]Park, C., *Nonequilibrium Hypersonic Aerothermodynamics*, Wiley, New York, 1990.

[14]Bird, G. A., "Nonequilibrium radiation during re-entry at 10 km/s," AIAA Paper No. 1987-1543, 1987.

[15]Carlson, A. B., and Hassan, H. A., "Radiation modeling with direct simulation Monte Carlo," *Journal of Thermophysics and Heat Transfer*, Vol. 8, 1994.

[16]Burt, J. M., and Josyula, E., "DSMC modeling of nonequilibrium electronic excitation and emission for hypersonic sensor applications," *45th AIAA Thermophysics Conference*, AIAA Paper No. 2015-2511, Dallas, TX, 2015.

[17]Ozawa, T., Li, Z., Sohn, I., Levin, D. A., and Modest, M. F., "Modeling of electronic excitation and radiation for hypersonic reentry flows in DSMC," *48th AIAA Aerospace Sciences Meeting*, AIAA Paper No. 2010-987, Orlando, FL, 2010.

[18]Liechty, D. S., and Lewis, M. J., "Extension of the Quantum-kinetic Model to Lunar and Mars Return Physics," *Physics of Fluids*, Vol. 26, No. 2, 2014.

[19]Boyd, I. D., "Monte Carlo simulation of nonequilibrium flow in a low-power hydrogen arcjet," *Physics of Fluids*, Vol. 9, 1997.

[20]Bird, G. A., *The DSMC Method*, G. A. Bird, 2013.

[21]Boyd, I. D., Beattie, D. R., and Cappelli, M. A., "Numerical and experimental investigations of low-density supersonic jets of hydrogen," *Journal of Fluid Mechanics*, Vol. 280, 1994.

[22]Takama, Y., and Suzuki, K., "Study on rotational relaxation in a steady hydrogen plasma jet using emission spectroscopy", *Journal of Thermophysics and Heat Transfer*, Vol. 24, No. 3, 2010.

[23]Liebowitz, L. P., and Kuo, T. J., "Ionizational Nonequilibrium Heating During Outer Planetary Entries," *AIAA Journal*, Vol. 14, No. 9, 1976, pp. 1324-1329.

[24]McBride, B. J., Zehe, M. J., and Gordon, S., "NASA Glenn Coefficients for Calculating Thermodynamic Properties of Individual Species," Glenn Research Center, NASA/TP-2002-211556, 2002.

[25]Park, C., "Nonequilibrium ionization and radiation in hydrogen-helium mixtures", *Journal of Thermophysics and Heat Transfer*, Vol. 26, No. 2, 2012.

[26]NIST online spectra database (http://physics.nist.gov/PhysRefData/ASD/levels_form.html)

[27]Gordon, S. and McBride, B. J., "Computer Program for Calculation of Complex Chemical Equilibrium Compositions and Applications," Lewis Research Center, NASA RP-1311, 1994.

Appendix A

Table A.1. Listing of electronic energy level information of atomic hydrogen.

Level j	$\varepsilon_{el,j}$ [J]	g_j	Level j	$\varepsilon_{el,j}$ [J]	g_j
0	0.000000000	2	20	$2.173767665\times10^{-18}$	882
1	$1.634032457\times10^{-18}$	8	21	$2.174204683\times10^{-18}$	968
2	$1.936631722\times10^{-18}$	18	22	$2.174582108\times10^{-18}$	1058
3	$2.042543054\times10^{-18}$	32	23	$2.174919804\times10^{-18}$	1152
4	$2.091568537\times10^{-18}$	50	24	$2.175217771\times10^{-18}$	1250
5	$2.118186911\times10^{-18}$	72	25	$2.175495873\times10^{-18}$	1352
6	$2.134237393\times10^{-18}$	98	26	$2.175714382\times10^{-18}$	1458
7	$2.144666234\times10^{-18}$	128	27	$2.175932891\times10^{-18}$	1568
8	$2.151817439\times10^{-18}$	162	28	$2.176111671\times10^{-18}$	1682
9	$2.156922605\times10^{-18}$	200	29	$2.176290452\times10^{-18}$	1800
10	$2.160696852\times10^{-18}$	242	30	$2.176449367\times10^{-18}$	1922
11	$2.163577198\times10^{-18}$	288	31	$2.176588418\times10^{-18}$	2048
12	$2.165821882\times10^{-18}$	338	32	$2.176707605\times10^{-18}$	2178
13	$2.167589819\times10^{-18}$	392	33	$2.176826792\times10^{-18}$	2312
14	$2.169020060\times10^{-18}$	450	34	$2.176926114\times10^{-18}$	2450
15	$2.170192063\times10^{-18}$	512	35	$2.177025437\times10^{-18}$	2592
16	$2.171165421\times10^{-18}$	578	36	$2.177124759\times10^{-18}$	2738
17	$2.171979864\times10^{-18}$	648	37	$2.177204217\times10^{-18}$	2888
18	$2.172675120\times10^{-18}$	722	38	$2.177283674\times10^{-18}$	3042
19	$2.173271054\times10^{-18}$	800	39	$2.177343268\times10^{-18}$	3200

Table A.2. Listing of electronic energy level information of diatomic hydrogen.

Level j	$\varepsilon_{el,j}$ [J]	g_j	Level j	$\varepsilon_{el,j}$ [J]	g_j
0	0.000000000	1	11	$2.247305890\times10^{-18}$	6
1	$1.821586712\times10^{-18}$	1	12	$2.247504534\times10^{-18}$	2
2	$1.903779881\times10^{-18}$	6	13	$2.255271538\times10^{-18}$	6
3	$1.905718652\times10^{-18}$	3	14	$2.255609233\times10^{-18}$	2
4	$1.987593990\times10^{-18}$	2	15	$2.262337325\times10^{-18}$	2
5	$1.988080669\times10^{-18}$	1	16	$2.262541929\times10^{-18}$	1
6	$2.140886028\times10^{-18}$	3	17	$2.340033181\times10^{-18}$	2
7	$2.217723739\times10^{-18}$	1	18	$2.343698173\times10^{-18}$	1
8	$2.238730403\times10^{-18}$	6	19	$2.361194788\times10^{-18}$	2
9	$2.241791516\times10^{-18}$	3	20	$2.370167564\times10^{-18}$	3
10	$2.242955573\times10^{-18}$	3	21	$2.407790848\times10^{-18}$	2

American Institute of Aeronautics and Astronautics

Table A.3. Listing of electronic energy level information of atomic helium.

Level j	$\varepsilon_{el,j}$ [J]	g_j	Level j	$\varepsilon_{el,j}$ [J]	g_j	Level j	$\varepsilon_{el,j}$ [J]	g_j
0	0.000000000	1	32	$3.847020509 \times 10^{-18}$	1	64	$3.878787750 \times 10^{-18}$	7
1	$3.175452837 \times 10^{-18}$	3	33	$3.849745912 \times 10^{-18}$	5	65	$3.878787750 \times 10^{-18}$	9
2	$3.303010469 \times 10^{-18}$	1	34	$3.849745912 \times 10^{-18}$	3	66	$3.878789737 \times 10^{-18}$	11
3	$3.358817678 \times 10^{-18}$	5	35	$3.849747899 \times 10^{-18}$	1	67	$3.878789737 \times 10^{-18}$	13
4	$3.358817678 \times 10^{-18}$	3	36	$3.852060122 \times 10^{-18}$	7	68	$3.878789737 \times 10^{-18}$	9
5	$3.358837542 \times 10^{-18}$	1	37	$3.852060122 \times 10^{-18}$	5	69	$3.878789737 \times 10^{-18}$	11
6	$3.399502075 \times 10^{-18}$	3	38	$3.852060122 \times 10^{-18}$	3	70	$3.879030097 \times 10^{-18}$	3
7	$3.639899762 \times 10^{-18}$	3	39	$3.852081973 \times 10^{-18}$	5	71	$3.890815680 \times 10^{-18}$	3
8	$3.672239100 \times 10^{-18}$	1	40	$3.852137593 \times 10^{-18}$	7	72	$3.893014675 \times 10^{-18}$	1
9	$3.686140248 \times 10^{-18}$	5	41	$3.852137593 \times 10^{-18}$	9	73	$3.893976115 \times 10^{-18}$	5
10	$3.686140248 \times 10^{-18}$	3	42	$3.852137593 \times 10^{-18}$	5	74	$3.893976115 \times 10^{-18}$	3
11	$3.686146207 \times 10^{-18}$	1	43	$3.852137593 \times 10^{-18}$	7	75	$3.893976115 \times 10^{-18}$	1
12	$3.696805475 \times 10^{-18}$	7	44	$3.852147525 \times 10^{-18}$	9	76	$3.894818368 \times 10^{-18}$	7
13	$3.696805475 \times 10^{-18}$	5	45	$3.852147525 \times 10^{-18}$	11	77	$3.894818368 \times 10^{-18}$	5
14	$3.696807462 \times 10^{-18}$	3	46	$3.852147525 \times 10^{-18}$	7	78	$3.894818368 \times 10^{-18}$	3
15	$3.696875001 \times 10^{-18}$	5	47	$3.852147525 \times 10^{-18}$	9	79	$3.894826314 \times 10^{-18}$	5
16	$3.698948851 \times 10^{-18}$	3	48	$3.852562693 \times 10^{-18}$	3	80	$3.894848165 \times 10^{-18}$	7
17	$3.780168661 \times 10^{-18}$	3	49	$3.872300018 \times 10^{-18}$	3	81	$3.894848165 \times 10^{-18}$	9
18	$3.792923630 \times 10^{-18}$	1	50	$3.875851783 \times 10^{-18}$	1	82	$3.894848165 \times 10^{-18}$	5
19	$3.798422112 \times 10^{-18}$	5	51	$3.877399225 \times 10^{-18}$	5	83	$3.894848165 \times 10^{-18}$	7
20	$3.798422112 \times 10^{-18}$	3	52	$3.877399225 \times 10^{-18}$	3	84	$3.894852138 \times 10^{-18}$	9
21	$3.798426084 \times 10^{-18}$	1	53	$3.877399225 \times 10^{-18}$	1	85	$3.894852138 \times 10^{-18}$	11
22	$3.802941276 \times 10^{-18}$	7	54	$3.878736103 \times 10^{-18}$	7	86	$3.894852138 \times 10^{-18}$	7
23	$3.802941276 \times 10^{-18}$	5	55	$3.878736103 \times 10^{-18}$	5	87	$3.894852138 \times 10^{-18}$	9
24	$3.802941276 \times 10^{-18}$	3	56	$3.878736103 \times 10^{-18}$	3	88	$3.894852138 \times 10^{-18}$	11
25	$3.802981005 \times 10^{-18}$	5	57	$3.878750008 \times 10^{-18}$	5	89	$3.894852138 \times 10^{-18}$	13
26	$3.803088273 \times 10^{-18}$	7	58	$3.878781791 \times 10^{-18}$	7	90	$3.894852138 \times 10^{-18}$	9
27	$3.803088273 \times 10^{-18}$	9	59	$3.878781791 \times 10^{-18}$	9	91	$3.894852138 \times 10^{-18}$	11
28	$3.803088273 \times 10^{-18}$	5	60	$3.878781791 \times 10^{-18}$	5	92	$3.894852138 \times 10^{-18}$	13
29	$3.803088273 \times 10^{-18}$	7	61	$3.878781791 \times 10^{-18}$	7	93	$3.894852138 \times 10^{-18}$	15
30	$3.803898743 \times 10^{-18}$	3	62	$3.878787750 \times 10^{-18}$	9	94	$3.894852138 \times 10^{-18}$	11
31	$3.840733408 \times 10^{-18}$	3	63	$3.878787750 \times 10^{-18}$	11	95	$3.894852138 \times 10^{-18}$	13

American Institute of Aeronautics and Astronautics

Table A.3. continued

Level j	$\varepsilon_{el,j}$ [J]	g_j	Level j	$\varepsilon_{el,j}$ [J]	g_j	Level j	$\varepsilon_{el,j}$ [J]	g_j
96	$3.895005094\times10^{-18}$	3	128	$3.911568079\times10^{-18}$	1	160	$3.917237396\times10^{-18}$	3
97	$3.902599276\times10^{-18}$	3	129	$3.912013043\times10^{-18}$	5	161	$3.917237396\times10^{-18}$	1
98	$3.904053355\times10^{-18}$	1	130	$3.912013043\times10^{-18}$	3	162	$3.917525430\times10^{-18}$	7
99	$3.904691004\times10^{-18}$	5	131	$3.912013043\times10^{-18}$	1	163	$3.917525430\times10^{-18}$	5
100	$3.904691004\times10^{-18}$	3	132	$3.912408346\times10^{-18}$	7	164	$3.917525430\times10^{-18}$	3
101	$3.904691004\times10^{-18}$	1	133	$3.912408346\times10^{-18}$	5	165	$3.917529403\times10^{-18}$	5
102	$3.905255154\times10^{-18}$	7	134	$3.912408346\times10^{-18}$	3	166	$3.917537349\times10^{-18}$	7
103	$3.905255154\times10^{-18}$	5	135	$3.912414305\times10^{-18}$	5	167	$3.917537349\times10^{-18}$	9
104	$3.905255154\times10^{-18}$	3	136	$3.912422251\times10^{-18}$	7	168	$3.917537349\times10^{-18}$	5
105	$3.905261114\times10^{-18}$	5	137	$3.912424237\times10^{-18}$	9	169	$3.917537349\times10^{-18}$	7
106	$3.905275019\times10^{-18}$	7	138	$3.912424237\times10^{-18}$	5	170	$3.917537349\times10^{-18}$	9
107	$3.905275019\times10^{-18}$	9	139	$3.912424237\times10^{-18}$	7	171	$3.917537349\times10^{-18}$	11
108	$3.905275019\times10^{-18}$	5	140	$3.912424237\times10^{-18}$	9	172	$3.917537349\times10^{-18}$	7
109	$3.905275019\times10^{-18}$	7	141	$3.912424237\times10^{-18}$	11	173	$3.917537349\times10^{-18}$	9
110	$3.905277005\times10^{-18}$	9	142	$3.912424237\times10^{-18}$	7	174	$3.917537349\times10^{-18}$	11
111	$3.905277005\times10^{-18}$	11	143	$3.912424237\times10^{-18}$	9	175	$3.917537349\times10^{-18}$	13
112	$3.905277005\times10^{-18}$	7	144	$3.912426224\times10^{-18}$	11	176	$3.917537349\times10^{-18}$	9
113	$3.905277005\times10^{-18}$	9	145	$3.912426224\times10^{-18}$	13	177	$3.917537349\times10^{-18}$	11
114	$3.905277005\times10^{-18}$	11	146	$3.912426224\times10^{-18}$	9	178	$3.917537349\times10^{-18}$	13
115	$3.905277005\times10^{-18}$	13	147	$3.912426224\times10^{-18}$	11	179	$3.917537349\times10^{-18}$	15
116	$3.905277005\times10^{-18}$	9	148	$3.912426224\times10^{-18}$	13	180	$3.917537349\times10^{-18}$	11
117	$3.905277005\times10^{-18}$	11	149	$3.912426224\times10^{-18}$	15	181	$3.917537349\times10^{-18}$	13
118	$3.905277005\times10^{-18}$	13	150	$3.912426224\times10^{-18}$	11	182	$3.917537349\times10^{-18}$	15
119	$3.905277005\times10^{-18}$	15	151	$3.912426224\times10^{-18}$	13	183	$3.917537349\times10^{-18}$	17
120	$3.905277005\times10^{-18}$	11	152	$3.912426224\times10^{-18}$	15	184	$3.917537349\times10^{-18}$	13
121	$3.905277005\times10^{-18}$	13	153	$3.912426224\times10^{-18}$	17	185	$3.917537349\times10^{-18}$	15
122	$3.905277005\times10^{-18}$	15	154	$3.912426224\times10^{-18}$	13	186	$3.917590983\times10^{-18}$	3
123	$3.905277005\times10^{-18}$	17	155	$3.912426224\times10^{-18}$	15	187	$3.921361257\times10^{-18}$	3
124	$3.905277005\times10^{-18}$	13	156	$3.912497736\times10^{-18}$	3	188	$3.924227699\times10^{-18}$	3
125	$3.905277005\times10^{-18}$	15	157	$3.916182593\times10^{-18}$	3	189	$3.926460464\times10^{-18}$	3
126	$3.905380301\times10^{-18}$	3	158	$3.916915591\times10^{-18}$	1	190	$3.928232373\times10^{-18}$	3
127	$3.910556978\times10^{-18}$	3	159	$3.917237396\times10^{-18}$	5	191	$3.929662614\times10^{-18}$	3

American Institute of Aeronautics and Astronautics

Table A.4. Listing of electronic energy level information of atomic helium ion.

Level j	$\varepsilon_{el,j}$ [J]	g_j	Level j	$\varepsilon_{el,j}$ [J]	g_j
0	0.000000000	2	20	$8.698523700\times10^{-18}$	882
1	$6.538719756\times10^{-18}$	8	21	$8.700279917\times10^{-18}$	968
2	$7.749593763\times10^{-18}$	18	22	$8.701812261\times10^{-18}$	1058
3	$8.173399596\times10^{-18}$	32	23	$8.703157085\times10^{-18}$	1152
4	$8.369561319\times10^{-18}$	50	24	$8.704343788\times10^{-18}$	1250
5	$8.476118246\times10^{-18}$	72	25	$8.705396207\times10^{-18}$	1352
6	$8.540368645\times10^{-18}$	98	26	$8.706333809\times10^{-18}$	1458
7	$8.582069704\times10^{-18}$	128	27	$8.707172685\times10^{-18}$	1568
8	$8.610659825\times10^{-18}$	162	28	$8.707926343\times10^{-18}$	1682
9	$8.631110086\times10^{-18}$	200	29	$8.708606105\times10^{-18}$	1800
10	$8.646241042\times10^{-18}$	242	30	$8.709220910\times10^{-18}$	1922
11	$8.657749317\times10^{-18}$	288	31	$8.709779101\times10^{-18}$	2048
12	$8.666705407\times10^{-18}$	338	32	$8.710287234\times10^{-18}$	2178
13	$8.673811917\times10^{-18}$	392	33	$8.710751268\times10^{-18}$	2312
14	$8.679544998\times10^{-18}$	450	34	$8.711175970\times10^{-18}$	2450
15	$8.684237182\times10^{-18}$	512	35	$8.711565909\times10^{-18}$	2592
16	$8.688125848\times10^{-18}$	578	36	$8.711924661\times10^{-18}$	2738
17	$8.691384613\times10^{-18}$	648	37	$8.712255404\times10^{-18}$	2888
18	$8.694142594\times10^{-18}$	722	38	$8.712561118\times10^{-18}$	3042
19	$8.696497327\times10^{-18}$	800	39	$8.712843988\times10^{-18}$	3200